A Structural Study of $La_{1-x}Y_xScO_3$, Combining Neutron Diffraction, Solid-State NMR and First-Principles DFT Calculations

Journal:	*The Journal of Physical Chemistry*
Manuscript ID:	jp-2012-10878b.R1
Manuscript Type:	Article
Date Submitted by the Author:	n/a
Complete List of Authors:	Johnston, Karen; University of St Andrews, School of Chemistry Mitchell, Martin; University of St Andrews, School of Chemistry Blanc, Frédéric; University of Cambridge, Chemistry Lightfoot, Philip; St Andrews University, Chemistry Ashbrook, Sharon; University of St Andrews, School of Chemistry

1
2
3
4
5
6
7
8
9
10
11
12
13
14
15
16
17
18
19
20
21
22
23
24
25
26
27
28
29
30
31
32
33
34
35
36
37
38
39
40
41
42
43
44
45
46
47
48
49
50
51
52
53
54
55
56
57
58
59
60

Alpo   A structural study of La$_{1-x}$Y$_x$ScO$_3$, combining neutron diffraction, solid-state NMR and first-principles DFT calculations

Karen E. Johnston,[1] Martin R. Mitchell,[1] Frédéric Blanc,[2] Philip Lightfoot*[1]
and Sharon E. Ashbrook*[1]

[1]School of Chemistry and EaStCHEM, University of St Andrews,

North Haugh, St Andrews, KY16 9ST, United Kingdom

[2]Department of Chemistry, Stony Brook University, Stony Brook,

New York, 11794-3400, USA

*Author to whom correspondence should be addressed.

Phone: +44 (0)1334 463779

Fax: +44 (0)1334 463808

Electronic mail: sema@st-andrews.ac.uk and pl@st-andrews.ac.uk

Abstract

The solid-solution $La_{1-x}Y_xScO_3$ (x = 0, 0.2, 0.4, 0.6, 0.8 and 1) has been successfully synthesized using conventional solid-state techniques. Detailed structural characterization has been undertaken using high-resolution neutron powder diffraction and multinuclear (^{45}Sc, ^{139}La, ^{89}Y and ^{17}O) solid-state NMR, and is supported by first-principles density functional theory calculations. Diffraction data indicates that a reduction in both the unit cell parameters and unit cell volume is observed with increasing x, and an orthorhombic perovskite structure (space group *Pbnm*) is retained across the series. ^{45}Sc multiple-quantum (MQ) MAS NMR spectra proved to be highly sensitive to subtle structural changes and, in particular, cation substitutions. NMR spectra of $La_{1-x}Y_xScO_3$ exhibited significant broadening, resulting from distributions of both quadrupolar and chemical shift parameters, owing to the disordered nature of the material. In contrast to previous single crystal studies, which reveal small deficiencies at both the lanthanide and oxygen sites, the powder samples studied herein are found to be stoichiometric.

Introduction

Oxides with the perovskite structure (general formula ABX_3) are an important and attractive area of research within materials chemistry. Perovskites are extremely flexible in their composition and, as a result, can be distorted with relative ease, producing a variety of useful and diverse physical properties including ferroelectricity, superconductivity, ionic conductivity and a range of dielectric responses, each of which can be exploited in a wide range of materials and devices. Although the 'ideal' perovskite structure is cubic, perovskites typically exhibit a range of structural variations owing to distortions or, more commonly, tilting of the BX_6 octahedra and displacements of the A- and B-site cations from the centre of their coordination polyhedra. Octahedral tilting is an intrinsic property of perovskites and is a direct consequence of the relative sizes and charge of the A- and B-site cations substituted into the structure. Both the type and magnitude of the distortions govern the nature and extent of the physical properties observed.

Stoichiometric ternary perovskite-type oxides of the form $LnBO_3$, where Ln and B are trivalent lanthanides and first row transition metals, respectively, have been studied extensively in the past with work concentrating predominantly on rare earth scandates, vanadates, gallates, orthochromates and orthoferrites.[1-7] Many of these compounds exhibit interesting physical properties which have led to important fundamental and industrial applications. In particular, the $LnScO_3$ series has found application in ionic conductivity[8] and as a substrate for ferroelectric thin films.[9] Liferovich and Mitchell[10] recently reinvestigated many ternary lanthanide orthoscandate perovskites and discovered much of the earlier literature regarding their structural behaviour to be correct. For example, many of the compounds investigated, including $LaScO_3$, were found to adopt the $GdFeO_3$ structure, which is isostructural with orthorhombic $CaTiO_3$.[4] The $LaScO_3$ structure, in space group *Pbnm*, contains corner sharing ScO_6 octahedra displaying significant octahedral tilting described, in Glazer notation, by the symbol $a^-a^-c^+$, with anti-phase tilts in the ab plane and in-phase tilts around the c axis, as shown in Figure 1.

The closely-related rare earth scandate $YScO_3$ has been investigated extensively in previous years and is well documented as requiring high-pressure techniques for successful synthesis.[10,11] Despite several attempts having been made to synthesize $YScO_3$ using conventional solid-state methods, many have been unsuccessful, as samples typically contain

only trace amounts of the desired perovskite and large quantities of different impurity phases.[11] The structure of $YScO_3$ was therefore unknown until recently, when Balamurugan *et al.* reported a single crystal study.[12] Using a flux technique originally used by Remeika *et al.*,[13] they were able to synthesize single crystals of both $LaScO_3$ and $YScO_3$. Their single crystal X-ray diffraction studies indicated small deficiencies in each structure on both the A site and oxygen sites, leading to compositions of $La_{0.94}ScO_{2.91}$ and $Y_{0.96}ScO_{2.94}$. In 1980, the first successful synthesis of $YScO_3$ using conventional solid-state techniques (a two-stage reaction under ambient pressure conditions) was reported by Portnikov *et al.*[14]

Clark[11] and co-workers identified a complex series of rare earth scandates that, in theory, should have produced perovskite-type structures. However, in reality they preferred to adopt 'C-type' solid-solutions, where preference for both the A- and B-site cations to be on the octahedral site is predominant. Under ambient pressure conditions and high annealing temperatures, many of the compounds investigated by Clark *et al.*, including $YScO_3$, contained trace amounts of the desired perovskite and large quantities of a C-type solid-solution. It was later discovered that it is possible to synthesize a phase pure sample of $YScO_3$ using high-pressure techniques.[11]

There are currently no known structural studies for the related solid-solution $La_{1-x}Y_xScO_3$. Owing to its small ionic radius, Y^{3+} substitution is feasible, as well as favourable, on both the A and B sites in the perovskite structure. The precise site of substitution is, however, influenced by each of the cations present in the structure. For example, Y^{3+} and Sc^{3+} have relatively small ionic radii (1.02 Å and 0.87 Å, respectively, for eight-coordinate cations)[15] when compared with (eight-coordinate) La^{3+} (1.18 Å).[15]

In recent years, the application of density functional theory (DFT) calculations has accelerated due to the advancement and modification of both hardware and software. Codes that exploit the inherent periodicity and translational symmetry of solids are an integral addition to the solid-state NMR community. Furthermore, the use of DFT calculations has aided with both the assignment and interpretation of often complex NMR spectra.

Here we present a comprehensive structural study of the rare earth orthoscandate perovskites $LaScO_3$, $YScO_3$ and the associated solid-solution $La_{1-x}Y_xScO_3$ at room temperature using a variety of complementary techniques, including high-resolution neutron powder diffraction (NPD), high-resolution solid-state ^{45}Sc, ^{89}Y and ^{17}O magic-angle spinning (MAS) NMR, ^{139}La wideline NMR and planewave DFT calculations. We confirm that the solid-

solution $La_{1-x}Y_xScO_3$ does not form any C-type solid-solutions across the series. Using ^{45}Sc and ^{89}Y NMR we have also confirmed that the solid-solution $La_{1-x}Y_xScO_3$ exhibits disorder, believed to result from random occupancy of the A-site cations within the structure.

Experimental and Computational Details

Synthesis and Characterization

$La_{1-x}Y_xScO_3$ samples were synthesized using conventional solid-state methods. Stoichiometric amounts of commercial La_2O_3 (Sigma-Aldrich, 99.99%), Y_2O_3 (Sigma-Aldrich, 99.999%) and Sc_2O_3 (Stanford Materials Ltd, 99.995%) were mixed and ground in an agate mortar and pestle with acetone as a mobile phase. Samples were pressed into pellets and heated at temperatures ranging from 1200 °C to 1450 °C. $LaScO_3$ was prepared using an annealing temperature of 1400 °C for 3 days.[10] $YScO_3$ was synthesized in a two-stage reaction, 1200 °C for 65 hours followed by 1450 °C for 7 days, with intermediate regrinds.[14] Samples in the series $La_{1-x}Y_xScO_3$ (x = 0.2, 0.4, 0.6 and 0.8) were synthesized by heating at 1450 °C for up to 4 days, with intermediate regrinding. After the initial solid-state preparation small quantities of $LaScO_3$ and $YScO_3$ were enriched using ^{17}O enriched O_2 gas. Enrichment was performed by heating the sample under 50% ^{17}O enriched O_2 gas (Isotec, 50% ^{17}O) for 7 days at 1000 °C. Samples were characterized by room temperature laboratory X-ray diffraction experiments (l-PXRD) using a Stoe STADI-P diffractometer using Cu K_{α_1} (λ = 1.54056 Å) radiation and time-of-flight neutron powder diffraction (NPD) using POLARIS at the ISIS neutron spallation source, Rutherford-Appleton Laboratories.[16,17] All diffraction data were analyzed by Rietveld refinement using the General Structure Analysis System (GSAS) software package.[18]

NMR Spectroscopy

Spectra were acquired using either Bruker 400 Avance I or 600 Avance III spectrometers, equipped with wide-bore 9.4 T and 14.1 T magnets, respectively using Larmor frequencies of 97.2 MHz and 145.8 MHz for ^{45}Sc (I = 7/2), 84.77 MHz for ^{139}La (I = 7/2), 29.41 MHz for ^{89}Y (I = 1/2) and 81.4 MHz for ^{17}O (I = 5/2). Powdered samples were packed into conventional 4- and 2.5-mm ZrO_2 rotors and MAS rates of 14 kHz and 30 kHz, respectively, were employed. Chemical shifts were referenced to 0.2 M $ScCl_3$ (aq), 1 M $LaCl_3$ (aq), 1 M YCl_3

(aq) and H_2O (aq), using $LaScO_3$ (s), $LaAlO_3$ (s), $Y_2Sn_2O_7$ (s) and 35% [17]O enriched clinohumite as secondary references.

Conventional [45]Sc MAS NMR spectra were obtained using single pulse experiments at 9.4 T and 14.1 T with typical pulse lengths of 1.25 µs and 1.4 µs, respectively. Conventional [89]Y and ^{17}O MAS NMR spectra were obtained using single pulse experiments at 14.1 T with typical $\pi/2$ pulse lengths of 8 µs and 1.5 µs, respectively. Experimentally optimized recycle intervals for [45]Sc, [89]Y and [17]O were 3 s, 20 s and 20 s, respectively. Typical radiofrequency field strengths of 30-60 kHz were employed. Two-dimensional triple-quantum [45]Sc MAS NMR experiments were acquired using a z-filtered pulse sequence,[19] and are the result of averaging 96 transients with a recycle interval of 3 s for each of the 256 increments of 20 µs. Spectra were not sheared post Fourier transformation. All spectral analysis and fitting was performed within Topspin 2.1.

A static wideline [139]La NMR spectrum was acquired in a piecewise manner using the WURST-QCPMG[20,21] pulse sequence, with a 50 µs WURST pulse swept over 1000 kHz (sweep rate of 20 MHz/ms). An experimentally optimized recycle interval of 2 s was used. Spectra were processed with exponential apodization, followed by digital filtering, Fourier transformation and magnitude calculation. The individual subspectra were then coadded to produce the final spectrum. Analytical simulations and spectral fitting of the [139]La spectrum was performed using WSolids.[22]

A static [89]Y NMR spectrum was acquired using a spin-echo pulse sequence. A half-echo was recorded and the FID was left shifted prior to Fourier transformation.

First-Principles Calculations

Planewave density functional theory (DFT) calculations were carried out using the CASTEP[23] DFT code, a planewave pseudopotential method that utilizes the gauge-including projector augmented wave (GIPAW) formalism. The generalized gradient approximation (GGA) PBE functional was used, with the core-valence interactions being described by ultrasoft pseudopotentials. Integrals over the Brillouin zone were performed using a Monkhorst-Pack grid with a k-point spacing of 0.04 Å^{-1}. Wavefunctions were expanded in planewaves, with a kinetic energy less than a cut-off energy, typically 60 Ry. Calculations were converged as far as possible with respect to both k-point spacing and cut-off energy. Calculations output both the absolute shielding tensor, σ, and the electric field gradient (EFG)

tensor, **V**, in the crystal frame. The isotropic chemical shift, δ_{iso}, can be obtained from the isotropic shielding, σ_{iso}, by $\delta_{iso} = -(\sigma_{iso} - \sigma_{ref})$ where σ_{ref} is a reference shielding, determined to be 788.0 ppm for ^{45}Sc, 2624.5 ppm for ^{89}Y, 223.7 ppm for ^{17}O and 4311.3 ppm for ^{139}La (from DFT calculations for LaScO$_3$, YScO$_3$ and LaAlO$_3$).[24] Crystal structures were obtained from both the Inorganic Crystal Structure Database (ICSD) and Rietveld refinement of experimental diffraction data. Where necessary, geometry optimization of the structure was performed (also using CASTEP) prior to the calculation of the NMR parameters, again using a k-point spacing of 0.04 Å^{-1} and a cut-off energy of 60 Ry. In a typical optimization, the forces and energy were converged using a tolerance of 5×10^{-2} eV/Å and 1×10^{-4} eV/atom, respectively. Calculations were performed using the EaStCHEM Research Computing Facility, consisting of 152 AMD Opteron processing cores partly connected by Infinipath high speed interconnects. Typical calculation times for single unit cell calculations ranged from 9 to 15 h for geometry optimization and 7 to 22 h for NMR calculations using 8 cores. Typical calculation times for supercell calculations ranged from 25 to 31 h for geometry optimization and 24 to 27 h for NMR calculations using 20 cores.

Referencing for ^{45}Sc

Experimental NMR

There is some degree of confusion in the literature regarding the most suitable primary NMR reference for ^{45}Sc. Several different reference compounds have been suggested previously, including Sc(NO$_3$)$_3$ (aq) and ScCl$_3$ (aq). To determine an accurate and reliable reference static ^{45}Sc NMR spectra were acquired for varying concentrations of Sc(NO$_3$)$_3$ (aq) (2, 1, 0.5, 0.2, 0.1, 0.05, 0.0375, 0.025, 0.0125 M) and ScCl$_3$ (aq) (0.2, 0.1, 0.075, 0.05, 0.04375, 0.0375, 0.025 M). All experimental parameters were optimized for 2 M Sc(NO$_3$)$_3$ (aq) and 0.2 M ScCl$_3$ (aq). Typical pulse lengths were 5 μs with recycle intervals of 0.5 s in each case.

Static ^{45}Sc NMR spectra were acquired for each solution and are shown in Figure S1 in the Supporting Information (referenced relative to the transmitter offset). The spectrum for 2 M Sc(NO$_3$)$_3$ (aq) displayed two resonances (Figure S1(a)). The spectrum for 1 M Sc(NO$_3$)$_3$ (aq) also exhibited two resonances. However, one of the resonances appears shifted relative to that observed for 2 M Sc(NO$_3$)$_3$ (aq). As the concentration was reduced a similar trend was observed, as the same resonance continued to shift until for 0.025 M and 0.0125 M Sc(NO$_3$)$_3$ (aq) only a single resonance was observed. Therefore, spectra acquired for Sc(NO$_3$)$_3$ (aq)

exhibited an obvious concentration dependent shift, most probably owing to hydration of the Sc and the varying number of H_2O molecules in the surrounding coordination environment. It is, therefore, not favourable to use $Sc(NO_3)_3$ (aq) as a primary reference.

The ^{45}Sc NMR spectrum for 0.2 M $ScCl_3$ (aq) displayed a single sharp resonance (Figure S1(b)). As the concentration of the solution was reduced the resonance position shifted. However, in contrast to $Sc(NO_3)_3$ (aq), a relatively small shift in peak position was observed as a function of concentration, suggesting $ScCl_3$ (aq) to be a more consistent and reliable reference. The single resonance displayed in the ^{45}Sc NMR spectrum for 0.2 M $ScCl_3$ (aq) was set to be 0 ppm. Using this, at 14.1 T, the resonance with maximum intensity in the spectrum of $LaScO_3$ was found at 162.91 ppm. $LaScO_3$ was then used as a solid secondary reference for ^{45}Sc, in subsequent experiments.

DFT Calculations

To establish the accuracy and feasibility of ^{45}Sc planewave DFT calculations using CASTEP initial calculations were completed on several 'model' compounds, including Sc_2O_3, $LiScO_2$, $NaScO_2$, $ScPO_4$ and $ScVO_4$. The calculated results were in excellent agreement with experimental data[25] as shown in Figure S2 in the Supporting Information.   The NMR parameters calculated for all model compounds displayed better correlation with experiment post geometry optimization of the structure. Similar calculations were completed for several Y-containing compounds, full details of which are given in ref 26. Each of the model compounds investigated displayed good agreement with the literature, confirming that the Sc and Y pseudopotentials used in each calculation were accurate for ^{45}Sc and ^{89}Y planewave DFT calculations using the CASTEP code.

Results and Discussion

LaScO₃

NPD and ^{45}Sc NMR

Several samples of $LaScO_3$ were synthesized to establish optimal reaction conditions. The structure and phase purity of each sample were verified using l-PXRD then NPD, both of which displayed excellent agreement with the orthorhombic structure (*Pbnm*) reported in the

literature.[10] In contrast to the findings of Balamurugan *et al.*,[12] there was no evidence in our l-PXRD or NPD data to suggest the presence of defects on the A site or oxygen sites. The Rietveld plots are shown in Figure S3 in the Supporting Information. Full refinement details obtained from the NPD data, including anisotropic thermal parameters, are given in Tables S1 and S2.

The ^{45}Sc (9.4 T) MAS NMR spectrum of $LaScO_3$ contained a single sharp resonance (Figure 2(a)). ^{45}Sc is a spin I = 7/2 nucleus with high natural abundance (100%) and a quadrupole moment Q(^{45}Sc) of -0.22×10^{-28} m^2. Despite being an extremely attractive nucleus to study by NMR there are, at present, relatively few publications in the literature demonstrating the use of ^{45}Sc solid-state NMR.[27] As a consequence, little is known regarding the relationship between the ^{45}Sc NMR parameters and local structure. A recent study by Kim *et al.*,[25] investigated the ^{45}Sc NMR isotropic chemical shifts, δ_{iso}, and quadrupolar coupling constants, C_Q, for a series of scandium-containing oxides. It was found that both quantities were sensitive to local structure. In particular, it was shown that ^{45}Sc δ_{iso} is largely dominated by coordination number. For example, a difference of more than 150 ppm was observed between shifts for six- and eight-coordinate scandium.

The ^{45}Sc (9.4 T and 14.1 T) MAS NMR spectra obtained for $LaScO_3$ (Figures 2(a) and (b), respectively) suggest the presence of a single six-coordinate site. Eight-coordinate scandium sites typically possess much lower chemical shifts when compared with six-coordinate Sc.[25] Each of the ^{45}Sc MAS NMR spectra of $LaScO_3$ exhibits a range of spinning sidebands (denoted by *) associated with the three satellite transitions; ST_1, ST_2 and ST_3 found for a I = 7/2 nucleus. These sidebands are better resolved in the ^{45}Sc (9.4 T) MAS NMR spectrum (Figure 2(c)). It is important to note the large anisotropic broadening associated with ST_3 when compared with ST_1 and ST_2. Tabulated in the Supporting Information (Table S3) are the values corresponding to the coefficients $A^0(7/2,q)$, $A^2(7/2,q)$ and $A^4(7/2,q)$ used to describe the second-order quadrupolar interaction for a transition, q.[28] A ^{45}Sc MAS NMR spectrum with a wide spectral width was also acquired for $LaScO_3$ at both 9.4 T and 14.1 T (Figures 2(e) and 2(f)) and in both the satellite transitions are clearly visible. This is in contrast to the ^{45}Sc MAS NMR data presented by Balamurugan *et al.*, where no satellite transitions were observed for $LaScO_3$.[12] The central and satellite transitions, ST_1, ST_2 and ST_3 were analytically simulated and fitted. The single Sc site has an isotropic chemical shift, δ_{iso} = 162.0 ppm, and a

quadrupolar coupling constant, C_Q = 3.9 MHz. Full details of the NMR parameters obtained for LaScO$_3$ are given in Table 1.

^{45}Sc is well documented as often exhibiting large quadrupolar coupling constants and, as a result, multiple-quantum (MQ) MAS techniques are often required to fully remove inhomogeneous second-order quadrupolar broadenings and resolve distinct resonances.[29,30] Therefore, to confirm no additional resonances were present in the ^{45}Sc MAS spectrum a MQMAS experiment was performed. The triple-quantum MAS spectrum (14. 1 T) is shown in Figure 3(a) and displays a single resonance, in good agreement with published crystallographic data.[10] Although the quadrupolar contribution appears to be relatively small, it is sufficiently large that one might expect to have observed a second-order quadrupolar lineshape at 9.4 T. However, the ^{45}Sc MAS NMR spectrum for LaScO$_3$ does not exhibit a well-defined quadrupolar lineshape, suggesting there is an additional degree of broadening present, most probably owing to factors such as small amounts of positional or geometrical disorder, most likely localized octahedral tilt disordering, an effect that is effectively averaged out in the diffraction data. This additional broadening is also observed in the MQMAS spectrum, as the single ridge is not aligned along 101/45 (+2.24) (the MQMAS ratio for a spin I = 7/2 nucleus) (*vide infra*).[31]

When compared with other scandium-containing compounds the quadrupolar interaction observed for LaScO$_3$ is relatively small, suggesting the Sc environment is more symmetrical. LaScO$_3$ is an orthorhombic perovskite composed of corner sharing ScO$_6$ octahedra, with the Sc cation directly bonded to six oxygen atoms. Crystallographically, Sc is positioned on an inversion centre. Therefore, by definition, the Sc should reside in the centre of the octahedron. However, the O – Sc – O bond angles obtained from the Rietveld refinement of LaScO$_3$ appear to indicate mild distortions of the octahedra (Tables S4 and S5 in the Supporting Information).

^{139}La and ^{17}O NMR

Lanthanum has two NMR active isotopes, ^{138}La (I = 5) and ^{139}La (I = 7/2). The latter is more favourable for NMR experimentation owing to its half-integer spin quantum number, higher natural abundance (99.91%) and smaller nuclear quadrupole moment (Q(^{138}La) = 0.45 × 10^{-28} m^2 and Q(^{139}La) = 0.20 × 10^{-28} m^2).[32] Solid-state ^{139}La NMR spectroscopy has been applied to a wide variety of systems, including simple lanthanum oxides and halides,[33,34] lanthanum-

containing zeolites and metallocenes,[35-39] and LaF$_3$ (both single crystals and nanoparticles).[40,41] Furthermore, the use of [139]La NMR has been demonstrated in perovskite solid-solution type systems such as La$_{1-x}$A$_x$MO$_3$, where A = Sr, Ca and M = Mn, Cr and Co.[42-45] Using the WURST-QCPMG pulse sequence[20,21] a static wideline [139]La NMR spectrum was acquired for LaScO$_3$ (14.1 T) and is shown in Figure S4 in the Supporting Information. The WURST-QCPMG pulse sequence combines the broadband excitation properties of frequency swept WURST pulses[46-48] with the signal-to-noise enhancement of the QCPMG protocol,[49,50] enabling the rapid acquisition of extremely broad powder patterns. The successful application of the WURST-QCPMG pulse sequence has been demonstrated several times in recent years for a variety of different systems, as part of numerous solid-state NMR studies.[51,52] The static [139]La powder pattern for LaScO$_3$ was best simulated with C$_Q$ = 62.5 MHz and η$_Q$ = 0.12. When compared with many other lanthanum-containing compounds the quadrupolar interaction for LaScO$_3$ is much larger, suggesting the spherical symmetry around the La atom is reduced. To highlight this reduction in symmetry an isolated cluster displaying the La environment, derived from the NPD Rietveld structure, is shown in the Supporting Information. Here, it is evident that the eight-coordinate A site exhibits a less symmetrical environment when compared to the six-coordinate B site, where an almost 'perfect' octahedron is found. The [139]La NMR parameters reflect these differences.

To gain additional structural information regarding the local environment of oxygen in LaScO$_3$ a sample was post-synthetically enriched using [17]O enriched O$_2$ gas. The structure and phase purity of the sample, post enrichment, were verified using l-PXRD. This confirmed the sample had not changed during the enrichment process. The ^{17}O MAS NMR spectrum (Figure 4) displays two distinct O sites, δ = 392.8 ppm and δ = 373.2 ppm, and is in good agreement with published crystallographic data.[10] Both sites exhibit small values of C$_Q$, suggesting each oxygen is in a spherically symmetric environment. A ^{17}O MAS NMR spectrum with a wide spectral width was also acquired and is shown in Figure S6(a) in the Supporting Information. The spectrum was fitted and the ^{17}O NMR parameters obtained are given in Table 1. To highlight how similar the two oxygen sites are, local oxygen environments for O1 and O2 are shown in Figure S7 with corresponding Sc – O and La – O bond distances highlighted.

First-Principles DFT Calculations

^{45}Sc, ^{139}La and ^{17}O NMR parameters were calculated for $LaScO_3$ using a structural model obtained from the literature,[10] and are given in Table 2. When compared with the experimentally obtained parameters (Table 1) very little agreement is observed between the two, highlighting the need for geometry optimization of the structure, *i.e.*, allowing both the unit cell and atomic coordinates to vary simultaneously. Better correlation with experiment was consistently observed for ^{45}Sc and ^{17}O post geometry optimization. All calculated values of the NMR parameters obtained prior to and post geometry optimization of the structure are given in Table 2. Also shown in the Supporting Information (Table S6) are the calculated parameters obtained post geometry optimization of the structure using a fixed unit cell, *i.e.*, allowing solely the atomic coordinates to vary. One major advantage of first-principles DFT calculations over experimental methods is their ability to determine the sign of C_Q. This information is automatically generated during each calculation.

YScO$_3$

NPD and ^{45}Sc NMR

A sample of $YScO_3$ was synthesized using the preparative method determined by Porotnikov *et al.*[14] The phase purity was verified using l-PXRD and high-resolution NPD. Each confirmed the presence of $YScO_3$, in addition to small quantities of an unknown impurity phase. Due to similarities in ionic radii at the A site, all Rietveld refinements for $YScO_3$ were carried out using the structural model for $HoScO_3$[10] as the starting point. The single phase Rietveld refinement completed for $YScO_3$ was in good agreement with the calculated model (wR$_P$ = 3.0 %), as shown in Figure S8 in the Supporting Information. Full refinement details obtained from the NPD data for $YScO_3$, including anisotropic thermal parameters, are also given in the Supporting Information (Tables S7 and S8). It was not possible to complete a multiphase Rietveld refinement for $YScO_3$ as the exact composition of the impurity phase was not known. The phase, believed to be a mixed $(Y,Sc)_2O_3$-type phase, is clearly visible in the refinement and denoted by *. Again, in contrast to the findings of Balamurugan *et al.*,[12] no evidence of A site or oxygen site defects were observed in our NPD data. It is possible that the synthetic procedure adopted by Balamurugan *et al.* gave rise to the defects observed. We also note that the present samples are white, whereas the samples from the previous study are pale yellow.

The ^{45}Sc (14.1 T) MAS NMR spectrum for YScO$_3$ contained a single resonance and, in contrast to LaScO$_3$, a characteristic second-order quadrupolar lineshape, as shown in Figure 3(b). As observed for LaScO$_3$, the chemical shift of the resonance was in the known chemical shift range for six-coordinate Sc.[25] The two-dimensional ^{45}Sc MQMAS NMR spectrum also displays a single six-coordinate site and confirms no additional resonances lie under the ^{45}Sc MAS NMR lineshape. The resonance appears to display a small amount of additional broadening under MAS, possibly indicative of small distributions in the environment and in the NMR parameters. The MAS lineshape for YScO$_3$ was fitted and the ^{45}Sc NMR parameters δ_{iso} = 163.3 ppm, C_Q = 7.6 MHz and η_Q = 0.7 were obtained. Full details of all NMR parameters are given in Table 1.

^{89}Y and ^{17}O NMR

^{89}Y is, in theory, an attractive proposition for study using NMR experimentation. However, as with ^{45}Sc there are some limitations to its practical use and implementation. ^{89}Y is a spin I = 1/2 nucleus with 100% natural abundance and large chemical shift range (~4000 ppm). However, it possesses an extremely low receptivity (0.681 relative to ^{13}C) and relaxation times are typically on the order of tens to thousands of seconds, meaning to obtain spectra of sufficiently high quality very long experimental times are required. One major advantage of ^{89}Y is that as a spin I = 1/2 nucleus it is free from the quadrupolar interaction and associated quadrupolar broadening.

A conventional ^{89}Y MAS NMR spectrum, slow spinning ^{89}Y MAS NMR spectrum and static ^{89}Y NMR spectrum were acquired for YScO$_3$ (14.1 T) and are shown in Figure 5. Fitting the slow spinning ^{89}Y MAS NMR spectrum for YScO$_3$ enables the isotropic chemical shift, δ_{iso}, the span, Ω, and skew, κ, to be determined. These parameters and their definitions are listed in Table 3.

YScO$_3$ was post-synthetically enriched using ^{17}O O$_2$ enriched gas. The structure and phase purity of the sample post enrichment was verified using l-PXRD. The ^{17}O MAS NMR spectrum (Figure 4(b)) displays two distinct O sites, δ = 334.5 ppm and δ = 310.5 ppm, and is in good agreement with the crystallographic data obtained from Rietveld refinement of the NPD data. Both sites exhibit relatively small values of C_Q, indicating the oxygen atoms are in a less symmetrical environment. The spectrum in Figure 4(b) was fitted and the NMR parameters obtained are given in Table 1. The two oxygen environments have similar values

of C_Q, indicating they are structurally very similar. To highlight how alike the two environments are isolated oxygen clusters for O1 and O2 in YScO$_3$ are shown in Figure S7 in the Supporting Information. When compared to the ^{17}O NMR parameters obtained for LaScO$_3$, the values of C_Q obtained for YScO$_3$ are larger, indicating these are less spherically symmetric than those in LaScO$_3$. This is particularly evident when the M – O bond distances are closely compared, as there is an obvious difference between the two phases. Owing to the nature of the perovskite structure, these differences are caused by different degrees of octahedral tilting and displacements of the A-site cation: both effects being more pronounced in the case of the smaller Y^{3+} cation.

DFT Calculations

As described previously for LaScO$_3$, ^{45}Sc, ^{89}Y and ^{17}O DFT calculations were completed for YScO$_3$. Owing to the lack of an exact crystal structure for YScO$_3$ structural models for HoScO$_3$ and LaScO$_3$ were used, in which the Ho and La atoms were replaced with Y. Each structure was fully optimized prior to calculation of the NMR parameters. The calculated parameters are given in Tables S11 and S12 in the Supporting Information and are in good agreement with those obtained experimentally. An additional DFT calculation was performed using the structural model obtained from Rietveld refinement of the NPD data for YScO$_3$. Parameters were calculated both prior to and post structural optimization. Interestingly, in this case the parameters calculated prior to optimization of the structure displayed reasonable agreement with the experimental parameters obtained, highlighting the accuracy of the Rietveld refinement obtained for YScO$_3$ (Table S13). Inspection of the atomic forces indicated very little change prior and post structural optimization, further indicating the accuracy of the structural model obtained. Full details of the calculated values prior to optimization and post structural optimization allowing solely the atomic coordinates to vary (*i.e.*, fixed unit cell) are given in the Supporting Information. The greatest agreement with experiment was consistently observed post geometry optimization of the structure.

Structural Comparison of LaScO$_3$ and YScO$_3$

The value of C_Q (for ^{45}Sc) for YScO$_3$ is ~5 MHz greater than that of LaScO$_3$. This suggests the Sc environment in YScO$_3$ is less spherically symmetric than that in LaScO$_3$. Both structures refine to the orthorhombic *Pbnm* structure, indicating the two are structurally very

similar. The Sc1 – O2 and Y1 – O1/O2 bond lengths in YScO$_3$ are marginally shorter than those in LaScO$_3$. In contrast, the Sc1 – O1 bond distances in YScO$_3$ are slightly longer than those in LaScO$_3$. To highlight the subtle differences between the two compounds, isolated ScO$_6$ octahedra of each, with corresponding bond distances, are shown in Figure 6. In contrast, larger differences are observed in the bond angles (O – Sc – O) obtained from Rietveld refinement of LaScO$_3$ and YScO$_3$, as detailed in the Supporting Information (Tables S5 and S10). The differences observed suggest that greater octahedral distortions are exhibited in YScO$_3$ when compared with LaScO$_3$. The small changes in bond length for LaScO$_3$ and YScO$_3$ do not appear sufficiently large enough to cause the large difference in C$_Q$ observed between the two. However, the differences in bond angle would be sufficient to cause such a large change.

Y^{3+} has a small ionic radius when compared with La^{3+} and, as a consequence, when Y^{3+} is substituted onto the A site the perovskite unit cell is forced to contract. This is confirmed by comparison of the lattice parameters obtained from refinement of the NPD data for each compound (Tables S1 and S7 in the Supporting Information). The substitution of a smaller cation onto the A site results in a higher degree of strain being imposed on the structure. To compensate, and relieve such strain from the structure, the A-site cation displaces and the surrounding octahedra undergo enhanced tilting. The degree of strain exhibited in any orthorhombic structure can be measured using an orthorhombic strain parameter, s, defined as 2(b – a)/(a + b), where a and b are the lattice parameters.[53] The orthorhombic strain found for LaScO$_3$ and YScO$_3$ are given in Table 4. As expected, s is greater for YScO$_3$ owing to the smaller size of the A-site cation. It is, therefore, likely that the large quadrupolar interaction exhibited by YScO$_3$ is due to several effects, namely the displacement of the A-site cation, pronounced tilting of the octahedra and an increase in the orthorhombic strain.

La$_{1-x}$Y$_x$ScO$_3$ Solid-Solution

NPD and ^{45}Sc NMR

Samples in the solid-solution La$_{1-x}$Y$_x$ScO$_3$, with composition x = 0.2, 0.4, 0.6 and 0.8, were synthesized using conventional solid-state methods. Structure and phase purity were initially verified using l-PXRD and later analyzed using NPD. All compositions in the solid-solution refined well to the orthorhombic *Pbnm* model. All Rietveld refinements are shown in Figures S9 and S10. Full refinement details obtained for each composition, including lattice

parameters, atomic coordinates, anisotropic thermal parameters, bond lengths and angles are given in the Supporting Information (Tables S15 – S26).

The NPD data indicates that the orthorhombic *Pbnm* structure was retained across the $La_{1-x}Y_xScO_3$ solid-solution. As the yttrium content was increased several important structural changes were observed. The lattice parameters a, b and c gradually decreased and, as a result, the unit cell volume reduced. The variation of each lattice parameter and cell volume with increasing Y content is shown in Figure 7(a). A near linear variation is observed with increasing x for both the lattice parameters and cell volume, in good agreement with Vegards Law. As Y is substituted into the structure the unit cell is forced to contract and, as a result, the orthorhombic strain imposed on the structure increases. A measure of the degree of octahedral tilting can be defined via the mean deviations of the Sc – O – Sc angles from 180 degrees, using the parameter φ, defined as $(180 - \langle Sc - O - Sc \rangle)/2$, where $\langle Sc - O - Sc \rangle$ is the average Sc – O – Sc bond angle obtained from Rietveld refinement.[53] In addition, it is possible to quantify the relative distortion of the octahedra in any perovskite structure using the parameter Δ_d.[53] This parameter, defined as $\Delta_d = 1/6[(d_n - \langle d \rangle)/\langle d \rangle]^2$, describes the deviation of the Sc – O distances (d_n) with respect to the average $\langle Sc - O \rangle$ value, $\langle d \rangle$, in each ScO_6 octahedron.[53] All values of s, ϕ and Δ_d obtained from Rietveld refinement of the NPD data for each sample in the series $La_{1-x}Y_xScO_3$ are given in Table 4. The variation of each parameter with composition is shown in Figures 7(b) and (c). As x is increased a gradual increase in both the orthorhombic strain and the degree of tilt of the ScO_6 octahedra is observed. This is in good agreement with earlier discussions regarding the placement of a smaller cation onto the A site, *i.e.*, the strain imposed on the structure increases owing to increased displacement of the A-site cation, coupled with enhanced rotations of the ScO_6 octahedra. The value of Δ_d also increases with increasing x, with a maximum observed for $YScO_3$. The values of Δ_d obtained for this solid-solution are extremely small when compared to those observed in other perovskite series such as $RMnO_3$, where the Jahn-Teller character of the Mn^{3+} produces a dramatic electronic driven distortion. For example, large octahedral distortions have been reported for $DyMnO_3$ at room temperature ($\Delta_d = 49.7$).[54]

The linear variation of each parameter calculated for the solid-solution $La_{1-x}Y_xScO_3$ confirms that a true solid-solution is formed between $LaScO_3$ and $YScO_3$. The trends exhibited also confirm that no phase transitions are observed with increasing x. Furthermore,

yttrium appears to be randomly distributed across the A site as there is no evidence of cation or layered ordering within the structure from diffraction.

It is evident from the NPD data that the substitution of Y^{3+} into the $LaScO_3$ structure introduces disorder into the system. Examination of the anisotropic thermal parameters obtained from each refinement indicates the largest values are exhibited for samples with compositions x = 0.4 and 0.6. This suggests that the greatest degree of disorder is exhibited between the two, presumably close to x = 0.5. Again, this perhaps suggests that the substitution of Y is random.

^{45}Sc (9.4 T and 14.1 T) MAS NMR spectra were acquired for all compositions in the series $La_{1-x}Y_xScO_3$, and are shown in Figures 8(a) and (b), respectively. Each spectrum displays a single resonance, suggesting the presence of a single Sc site. As observed for $LaScO_3$ and $YScO_3$ the isotropic chemical shift of each resonance is indicative of a six-coordinate site. In each, the central transition appears broadened and shifted relative to $LaScO_3$. In addition, a degree of asymmetric broadening is observed with a characteristic 'tail' to low frequency, indicating the presence of disorder and a distribution of NMR parameters.[55] The extent of broadening displayed in the ^{45}Sc MAS NMR spectra increases with increasing Y content. Spectra acquired at 14.1 T for each composition in this series have been overlaid to highlight the extent of broadening exhibited as x increases and are shown in Figure S11 in the Supporting Information. When the ^{45}Sc MAS NMR spectra acquired for $La_{1-x}Y_xScO_3$ are compared with that of $YScO_3$ it is evident that as greater quantities of Y^{3+} are added to the system a structure more similar to $YScO_3$ is adopted. The broad ^{45}Sc MAS NMR spectra and large quadrupolar interactions exhibited for the latter samples in the series are believed to be a result of increased stress and strain on the structure and is in good agreement with the NPD data.

To gain resolution and insight into the nature and extent of disorder exhibited in the $La_{1-x}Y_xScO_3$ series, MQMAS experiments were performed for each. The triple-quantum ^{45}Sc MAS spectrum for $La_{0.8}Y_{0.2}ScO_3$ is shown in Figure 9(a), displaying a single ridge and indicating the presence of a single Sc site, in good agreement with the NPD data. If no disorder is present in a system the ridge observed in any z-filtered experiment (prior to shearing) will be aligned along a gradient equal to the MQMAS ratio, R, *i.e.*, for a I = 7/2 nucleus the ridge will be aligned along 101/45 (+2.24).[31] When disorder is present the direction along which the ridge is broadened changes depending on the precise nature of the

disorder. For example, when a distribution of chemical shifts is present the centre of gravity for each environment will lie along a gradient of +3. If, however, a distribution of quadrupoles is present this alignment will be along a gradient of +1.8. In reality, many disordered systems exhibit contributions from both a distribution of chemical and quadrupolar shift interactions and, in such cases, the ridge will be broadened along more than one axis. To illustrate the effect disorder can have on the ridges in a MQMAS spectrum, MQMAS spectra have been simulated exhibiting each of these contributions and are shown in Figure S12 in the Supporting Information.

The single ridge in the ^{45}Sc MQMAS spectrum of $La_{0.8}Y_{0.2}ScO_3$ appears to be aligned along a gradient of +2.24. However, the ridge does exhibit a degree of additional broadening that is characteristic of disorder. The broadening is believed to be caused by a distribution of chemical and/or quadrupolar shift interactions. The ridge does not appear to be predominantly aligned along any one axis, suggesting the disorder is caused by a distribution of *both* chemical and quadrupolar shift interactions. As observed for $LaScO_3$, the ridge is relatively narrow. It is, therefore, difficult to quantify the disorder resulting from each distribution in any more detail.

Two-dimensional ^{45}Sc MAS NMR spectra were acquired for all remaining samples in the $La_{1-x}Y_xScO_3$ series and are shown in Figures 9(b) – (d). All spectra exhibit a single broadened ridge. For compositions $La_{0.6}Y_{0.4}ScO_3$ and $La_{0.4}Y_{0.6}ScO_3$ the ridges appear to be aligned along +2.24 with a small amount of additional broadening. As observed for the x = 0.2 sample, the disorder exhibited in each sample is believed to result from both a distribution of quadrupoles and chemical shifts. This is in good agreement with earlier discussions regarding the increase in orthorhombic strain and tilt angle producing a substantial change in the local coordination environment of the Sc and hence the quadrupolar interaction. To aid in the understanding and interpretation of the ^{45}Sc MQMAS spectra acquired for each sample and to obtain information regarding both the quadrupolar and chemical shift interactions, the position of the centre of gravity of the ridge lineshape (δ_1, δ_2) was obtained. This enabled the average chemical shift, $\langle\delta_{iso}\rangle$, and average quadrupolar product, $\langle P_Q\rangle$, to be determined. Details of these parameters, including a plot highlighting the variation in $\langle\delta_{iso}\rangle$ and $\langle P_Q\rangle$ with increasing x are given in the Supporting Information (Figure S13 and Table S27). It was found that $\langle P_Q\rangle$ gradually increases with increasing x, whilst $\langle\delta_{iso}\rangle$ reaches a maximum at x = 0.4.

To gain insight into the disorder exhibited in the $La_{1-x}Y_xScO_3$ series conventional [89]Y MAS NMR spectra were acquired for compositions x = 0.2, 0.4, 0.6 and 0.8. All [89]Y spectra exhibited a single resonance, from which no fingerprint of short range cation distribution is observed (Figure 10).[26,56] As x was increased a shift in $\langle\delta_{iso}\rangle$ was exhibited. The known chemical shift range for [89]Y is extremely large (~4000 ppm). However, the shift exhibited in this particular series was very small (121 ppm), suggesting a relatively small change is observed in the local Y environment. All values of $\langle\delta_{iso}\rangle$ extracted from the [89]Y MAS NMR spectra acquired and the variation observed in $\langle\delta_{iso}\rangle$ with increasing x are given in the Supporting Information (Figure S14 and Table S28). In a similar manner to the [45]Sc MAS NMR spectra acquired, compositions x = 0.2, 0.4, 0.6 and 0.8 exhibited broadening of the lineshape, most likely caused by the disorder of Y across the A site. The linewidth, $\Delta v_{1/2}$, of each [89]Y spectrum was also measured as a function of x and all values of $\Delta v_{1/2}$ extracted from the [89]Y MAS NMR spectra acquired are given in the Supporting Information. For I = 1/2 nuclei it is considerably easier to quantify the disorder present in any system, as the magnitude of the linewidth is expected to be directly proportional to disorder. The trend exhibited in $\Delta v_{1/2}$ for the $La_{1-x}Y_xScO_3$ series suggests the maximum level of disorder is close to x = 0.4 (as illustrated in the Supporting Information). This, in conjunction with the large anisotropic thermal parameters obtained from Rietveld refinement of the NPD data, indicates that the greatest disorder would be exhibited close to x = 0.5. This is as expected if Y is randomly distributed across the A site.

The substitution of Y^{3+} into the $LaScO_3$ structure appears to produce a greater effect on the local environment of the Sc, suggesting that the B site is more sensitive to changes occurring on the A site. From close inspection of the La – Y/La and Sc – Y/La distances it is apparent that the distance between the A- and B-site cations is smaller than the distance between two A-site cations. The B-site is therefore 'closer' to the A-site and, as a result, is more sensitive to any structural substitutions. The Y environment in $La_{1-x}Y_xScO_3$ would therefore experience a greater effect if Sc was substituted with an isovalent cation. This is in good agreement with both the [45]Sc and [89]Y MAS NMR data. Furthermore, the [45]Sc and [89]Y MAS NMR data confirm no phase transitions occur in this series and an orthorhombic structure is retained throughout, in good agreement with the NPD data.

DFT Calculations

To gain further insight into the disorder exhibited in the $La_{1-x}Y_xScO_3$ series several planewave DFT calculations were performed. Calculations were completed with (a) a single La atom, (b) two La atoms and (c) three La atoms in the $LaScO_3$ unit cell being replaced by Y atom(s), producing structures with compositions $La_{0.75}Y_{0.25}ScO_3$, $La_{0.5}Y_{0.5}ScO_3$ and $La_{0.25}Y_{0.75}ScO_3$, respectively. Structures for each composition are given in the Supporting Information (Figure S15). All structures were geometry optimized prior to calculation of the NMR parameters. The ^{45}Sc and ^{89}Y parameters calculated for each composition are given in the Supporting Information (Tables S29 and S30). The number of Sc and Y sites observed for each composition varied as a function of symmetry. Furthermore, for each composition a range of values of C_Q were predicted for ^{45}Sc that varied from ~5 – 12 MHz, as detailed in the Supporting Information. Several of the predicted values of C_Q were extremely large and would therefore result in very broad experimental resonances. To determine whether any of the calculated compositions could, realistically, be observed experimentally the values for each composition were 'summed', *i.e.*, their contributions were added and a corresponding spectrum was simulated (shown in blue in Figure 11(a)). When compared to the broad ^{45}Sc MAS NMR spectra obtained for samples in the $La_{1-x}Y_xScO_3$ series relatively good agreement was observed in both the position (shifted upfield from $LaScO_3$) and the shift range observed. This suggests that all possible compositions simulated using DFT methods are potentially present in each of the samples synthesized.

The ^{89}Y NMR parameters calculated for each composition also indicated a range of chemical shifts, as detailed in the Supporting Information. To determine whether any of these shifts were observed experimentally NMR spectra for each were simulated and compared with the observed experimental resonances. Tick marks corresponding to each of the calculated shifts have been added to the ^{89}Y MAS NMR spectrum of $La_{0.6}Y_{0.4}ScO_3$, and are shown in Figure 11(b). The range predicted using DFT are in good agreement with those seen experimentally and suggests that each type of environment could potentially be present in the material.

In reality, to gain a more accurate understanding of the disorder exhibited DFT calculations using much larger cells are required. Using a supercell approximation and inherent periodic boundary conditions of each system, the structure can be extended in three dimensions by a greater number of unit cells. A 2 × 2 × 2 supercell extends the structure in each of the three dimensions by an additional unit cell. Calculations of this type are,

however, computationally demanding and often require large computational resources. A $2 \times 1 \times 1$ supercell calculation was therefore performed using the computational resources currently available to us. Initially, a single La atom was replaced in the $2 \times 1 \times 1$ cell with Y, producing the composition $La_{0.875}Y_{0.125}ScO_3$, as shown in the Supporting Information (Figure S16). As with all calculations of this nature, the structure was fully geometry optimized prior to calculation of the NMR parameters. The calculated ^{45}Sc and ^{89}Y NMR parameters are given in the Supporting Information (Tables S31 and S32). Calculations were also attempted substituting two La atoms in the $2 \times 1 \times 1$ cell with Y, producing the composition $La_{0.75}Y_{0.25}ScO_3$. The calculated ^{45}Sc and ^{89}Y NMR parameters are given in Tables S31 and S32, respectively. As observed for the single cell calculations, the number of sites predicted varied as a function of symmetry and a large range of quadrupolar coupling constants ($C_Q = 4 - 14$ MHz) were predicted for each Sc site. The contribution from each of these sites was 'summed' and the resulting spectrum is denoted in purple in Figure 11(a). The simulated spectrum again highlights that each environment calculated could realistically be present in each sample. Also shown in Figure 11(a), and denoted in green, is the summation of the two simulated spectra (blue and purple). The same upfield shift from $LaScO_3$ is observed and is generally in good agreement with experimental findings. As previously observed for the single cell calculations, a range of ^{89}Y NMR chemical shifts were predicted. To illustrate whether any of these sites could be potentially present experimentally, tick marks corresponding to each shift have been added to the ^{89}Y MAS NMR spectrum for $La_{0.6}Y_{0.4}ScO_3$, and are shown in Figure 11(b). The range of chemical shifts are relatively small and indicate that each resonance could reside under the experimental lineshape. To obtain a more realistic representation of the disorder present in each sample larger supercell calculations are needed but these are beyond our present computational resources.

Conclusions

In summary, we have successfully synthesized and characterized the $La_{1-x}Y_xScO_3$ solid-solution for compositions x = 0, 0.2, 0.4, 0.6, 0.8 and 1 using high-resolution NPD, multinuclear solid-state NMR and planewave DFT calculations. All samples in the series were found to be orthorhombic and isostructural with $GdFeO_3$, in space group $Pbnm$. As Y^{3+}

was gradually introduced to the $LaScO_3$ structure a corresponding decrease in both the lattice parameters and unit cell volume was observed. In addition, as x was increased the incorporation of the smaller A-site cation led to corresponding increases in both orthorhombic strain and the degree of octahedral tilting. Structurally, minor changes in the Sc – O bond lengths were observed as x increased. In addition, as these strain effects increased a substantial influence on the magnitude of the quadrupolar interaction was observed. A complete structural model (obtained from NPD data) was reported for $YScO_3$ and is in contrast to the findings of Balamurugan *et al.*,[12] as no defects were observed on the A site or oxygen sites within the structure.

^{45}Sc MAS NMR was shown to be sensitive to substitutions occurring on the A site. In contrast, the ^{89}Y MAS NMR spectra indicated the Y environment to be less sensitive to changes on the A site. The local environment of the Sc was therefore more sensitive to cation substitution on the A site, owing to the close proximity of the Sc to a substituted La atom. Each sample in the $La_{1-x}Y_xScO_3$ series exhibited disorder and using two-dimensional ^{45}Sc MAS NMR it was found to result from a distribution of both quadrupolar and chemical shift parameters. Using ^{45}Sc and ^{89}Y MAS NMR, in conjunction with high-resolution NPD data, the greatest disorder was found to be at compositions close to x = 0.5, as expected if cation substitution is random.

In addition, we completed a series of planewave DFT calculations to gain insight into the disorder exhibited in the $La_{1-x}Y_xScO_3$ series. Initial calculations were successful and suggested a variety of different compositional environments could be present in each sample. This is in good agreement with the random A site occupancies evidenced by both diffraction and NMR. It is highly likely that, experimentally, a 'summation' of all the calculated environments is observed (again a good indication of the random nature of the disorder). Preliminary calculations suggest that 'modelling' disorder using DFT could aid considerably in the understanding and interpretation of complex NMR spectra of disordered materials.

We, therefore, emphasise the importance of using a multidisciplinary approach to the structural investigation of complex solid-state systems such as $La_{1-x}Y_xScO_3$. Using a variety of highly complementary techniques it is possible to gain important additional structural information that may be lost by the use of a single technique alone.

1
2
3
4
5
6
7
8
9
10
11
12
13
14
15
16
17
18
19
20
21
22
23
24
25
26
27
28
29
30
31
32
33
34
35
36
37
38
39
40
41
42
43
44
45
46
47
48
49
50
51
52
53
54
55
56
57
58
59
60

Acknowledgments

Supporting Information Available

Additional Rietveld refinements, bond distances and angles obtained from Rietveld refinements and calculated ^{45}Sc, ^{139}La, ^{89}Y and ^{17}O NMR parameters (using CASTEP) is available free of charge via the Internet at http://pubs.acs.org.

Table 1: Experimental NMR parameters, δ_{iso}, P_Q, C_Q and η_Q, for LaScO$_3$ (9.4 T) and YScO$_3$ (14.1 T). Also given are the CSA parameters, Ω and κ, obtained from the static spectrum in Figure S4.

	Site	δ_{iso} (ppm)	P_Q / MHz[a]	C_Q / MHz[b]	η_Q[c]	Ω (ppm)[d]	κ[e]
LaScO$_3$	Sc1	162.0(5)	4.0(1)	3.9(1)	0.3(1)	-	-
	La1	600(50)	61.7(5)	61.6(5)	0.10(2)	500(200)	0.0(3)
	O1	393.1(5)	0.57(1)	0.56(1)	0.3(1)	-	-
	O2	374.3(5)	1.10(1)	1.09(1)	0.2(1)	-	-
YScO$_3$	Sc1	163.2(5)	8.2(1)	7.6(1)	0.7(1)	-	-
	O1	335.8(5)	1.33(1)	1.33(1)	0.09(1)	-	-
	O2	312.1(5)	1.29(1)	1.29(1)	0.1(1)	-	-

$^{a}P_Q = C_Q(1 + (\eta_Q)^2/3)^{1/2}$ $^{b}C_Q = eQV_{33}/h$ $^{c}\eta_Q = (V_{11} - V_{22})/V_{33}$ $^{d}\Omega = \delta_{11} - \delta_{33}$ $^{e}\kappa = 3(\delta_{22} - \delta_{iso})/\Omega$

Table 2: Calculated (using CASTEP) ^{45}Sc and ^{17}O NMR parameters (δ_{iso}, P_Q, C_Q and η_Q) for LaScO$_3$ obtained (a) prior to and (b) post full geometry optimization of the structure.

	Site	δ_{iso} (ppm)	P_Q / MHz[a]	C_Q / MHz[b]	η_Q[c]
$^{(a)}$LaScO$_3$	Sc1	160.8	6.49	5.89	0.80
	La1	129.2	−57.93	−57.91	0.04
	O1	375.0	−0.80	−0.80	0.17
	O2	360.0	−1.34	−1.32	0.31
$^{(b)}$LaScO$_3$	Sc1	162.0	3.96	3.70	0.66
	La1	88.5	−51.81	−51.66	0.13
	O1	381.2	−0.68	−0.68	0.17
	O2	365.6	−1.28	−1.26	0.28

$^{a}P_Q = C_Q(1 + (\eta_Q)^2/3)^{1/2}$ $^{b}C_Q = eQV_{33}/h$ $^{c}\eta_Q = (V_{11} - V_{22})/V_{33}$.

Table 3: ^{89}Y NMR parameters, δ_{iso}, Ω and κ, for YScO$_3$ obtained from fitting of the slow spinning MAS spectrum shown in Figure 5.

	δ_{iso} (ppm)	Ω / ppm[a]	κ[b]
YScO$_3$	263.1(5)	−221(4)	0.33(5)

$\cdot\Omega = \delta_{11} - \delta_{33}$ $^b\kappa = 3(\delta_{22} - \delta_{iso})/\Omega$

Table 4: The values of s, φ and Δ_d, obtained for the solid-solution La$_{1-x}$Y$_x$ScO$_3$.

x	s[a]	ϕ (°)[b]	Δ_d ($\times 10^4$)[c]
0	0.019	15.5	0.099
0.2	0.025	16.4	0.051
0.4	0.032	17.4	0.119
0.6	0.038	18.5	0.183
0.8	0.044	19.6	0.414
1	0.051	20.4	0.878

[a]The orthorhombic strain is defined as s = 2(b − a)/(a + b) [b]ϕ = (180 − ⟨Sc − O − Sc⟩)/2 [c]Δ_d = 1/6([(d$_n$ − ⟨d⟩)/⟨d⟩]^2)[53]

References

1.   Keith, M. L.; Roy, R. *Am. Mineral.* **1954**, *39*, 1.

2.   Geller, S.; Wood, E. A. *Acta Cryst.* **1956**, *9*, 563.

3.   Geller, S.; Bala, V. B. *Acta Cryst.* **1956**, *9*, 1019.

4.   Geller, S. *J. Chem. Phys.* **1956**, *24*, 1236.

5.   Gilleo, M. A. *Acta Cryst.* **1957**, *10*, 161.

6.   Geller, S. *Acta Cryst.* **1957**, *10*, 243.

7.   Schneider, S. J.; Roth, R. S.; Waring, J. L. *J. Res. Nat. Bur. Stand. A* **1961**, *65*, 345.

8.   Lybye, D.; Bonanos, N. *Solid State Ionics* **1999**, *125*, 339.

9.   Pabst G. W.; Martin, L. W.; Chu, Y.-H.; Ramesh, R. *Appl. Phys. Lett.* **2007**, *90*, 072902.

10.   Liferovich, R. P.; Mitchell, R. H. *J. Solid State Chem.* **2004**, *177*, 2188.

11.   Clark, J. B.; Richter, P. W.; Du Toit, L. *J. Solid State Chem.* **1978**, *23*, 129.

12.   Balamurugan, S.; Rodewald, U.; Harmening, T.; van Wüllen, L.; Mohr, D.; Deters, H.; Eckert, H.; Pöttgen, R. *Z. Naturforsch* **2010**, *65*, 1199.

13.   Remeika, J. P. *J. Am. Chem. Soc.* **1956**, *78*, 4259.

14.   Porotnikov, N. V.; Petrov, K. I.; Tsygankov, V. N; Bogdanova, M. E. *Inorg. Mater. (Transl. of Neorg. Mater.)* **1980**, *16*, 62.

15.   Shannon, R. D. *Acta Cryst.* **1976**, *A32*, 751.

16   Smith, R. I.; Hull, S.; Armstrong, A. R. *Mater. Sci. Forum* **1993**, *166*, 251.

17.   Hull, S.; Smith, R. I.; David, W. I. F.; Hannon, A. C.; Mayers, J.; Cywinski, R. *Physica B* **1992**, *180*, 1000.

18.   Larson, A. C.; von Dreele, R. B. Report No. LA-UR-86-748; Los Alamos National Laboratory: Los Alamos, NM, 1987.

19.   Fernandez, C.; Amoureux, J.-P. *Solid State Nucl. Magn. Reson.* **1996**, *5*, 315.

20.   O'Dell, L. A.; Schurko, R. W. *Chem. Phys. Lett.* **2008**, *464*, 97.

21.   O'Dell, L. A.; Rossini, A. J.; Schurko, R. W. *Chem. Phys. Lett.* **2009**, *468*, 330.

22.   Eichele, K.; Wasylishen, R. E. *WSolids: Solid-State NMR Spectrum Simulation Package*; 2001.

23.   Clark, S. J.; Segall, M. D.; Pickard, C. J.; Hasnip, P. J.; Probert, M. I. J.; Refson, K.; Payne, M. C. *Z. Kristallogr.* **2005**, *220*, 567.

24.   Middlemiss, D. S.; Blanc, F.; Pickard, C. J.; Grey, C. P. *J. Magn. Reson.* **2010**, *204*, 1.

25. Kim, N.; Hsieh, C.-H.; Stebbins, J. F. *Chem. Mater.* **2006**, *18*, 3855.

26. Reader, S. W.; Mitchell, M. R.; Johnston, K. E.; Pickard, C. J.; Whittle, K. R.; Ashbrook, S. E. *J. Phys. Chem. C* **2009**, *113*, 18874.

27. Eckert, H.; Pöttgen, R. *Z. Anorg. Allg. Chem.* **2010**, *636*, 2232.

28. Ashbrook, S. E.; Wimperis, S. *Prog. Nucl. Magn. Reson. Spectrosc.* **2004**, *45*, 53.

29. Smith, M. E.; van Eck, E. R. H. *Prog. NMR Spectrosc.* **1999**, *34*, 159.

30. Thompson, A. R.; Oldfield, E. *J. Chem. Soc. Chem. Commun.* **1987**, *1*, 27.

31. Amoureux, J.-P.; Fernandez, C. *Solid State Nucl. Magn. Reson.* **1998**, *10*, 211.

32. Pyykko, P. *Mol. Phys.* **2001**, *99*, 1617.

33. Bastow, T. J. *Z. Naturforsch., A: Phys. Sci.* **1994**, *49*, 320.

34. Ooms, K. J.; Feindel, K. W.; Willans, M. J.; Wasylishen, R. E.; Hanna, J. V.; Pike, K. J.; Smith, M. E. *Solid State Nucl. Magn. Reson.* **2005**, *28*, 125.

35. Hunger, M.; Engelhardt, G.; Weitkamp, J. *Stud. Surf. Sci. Catal.* **1994**, *84*, 725.

36. Engelhardt, G.; Hunger, M.; Koller, H.; Weitkamp, J. *Stud. Surf. Sci. Catal.* **1994**, *84*, 421.

37. Hunger, M.; Engelhardt, G.; Weitkamp, J. *Micoporous Mater.* **1995**, *3*, 497.

38. Herreros, B.; Man, P. P.; Manoli, J. M.; Fraissard, J. *J. Chem. Soc., Chem. Commun.* **1992**, 464.

39. Hamaed, H.; Lo, A. Y. H.; Lee, D. S.; Evans, W. J.; Schurko, R. W. *J. Am. Chem. Soc.* **2006**, *128*, 12638.

40. L. O.; Proctor, W. G. *Z. Kristallogr.* **1968**, *127*, 366.

41. Lo, A. Y. H.; Sudarsan, V.; Sivakumar, S.; van Veggel, F.; Schurko, R. W. *J. Am. Chem. Soc.* **2007**, *129*, 4687.

42. Savosta, M. M.; Doroshev, V. D.; Kamenev, V. I.; Borodin, V. A.; Tarasenko, T. N.; Mazur, A. S.; Marysko, M. *J. Exp. Theor. Phys.* **2003**, *97*, 573.

43. Papavassiliou, G.; Fardis, M.; Milia, F.; Pissas, M.; Kallias, G.; Niarchos, D.; Dimitropoulos, C.; Scherrer, P. *Phys. Rev. B* **1998**, *58*, 12237.

44. Bastow, T. J. *Solid State Nucl. Magn. Reson.* **1994**, *3*, 17.

45. Hoch, M. J. R.; Kuhns, P. L.; Moulton, W. G.; Reyes, A. P.; Lu, J.; Wu, J.; 57. Leighton, C. *Phys. Rev. B* **2004**, *70*, 174443/1.

46. Kupce, E.; Freeman, R. *J. Magn. Reson. A* **1995**, *115*, 273.

47. Kupce, E.; Freeman, R. *J. Magn. Reson. A* **1996**, *118*, 299.

48. Bhattacharyya, R.; Frydman, L. *J. Chem. Phys.* **2007**, *127*, 194503.

49. Larsen, F. H.; Jakobsen, H. J.; Ellis, P. D.; Nielsen, N. C. *J. Magn. Reson.* **1998**, *131*, 144.

50. Larsen, F. H.; Jakobsen, H. J.; Ellis, P. D.; Nielsen, N. C. *J. Phys. Chem. A* **1997**, *101*, 8597.

51. O'Dell, L. A.; Schurko, R. W. *J. Am. Chem. Soc.* **2009**, *131*, 6658.

52. Hamaed, H.; Ye, E.; Udachin, K; Schurko, R. W. *J. Phys. Chem. B* **2010**, *114*, 6014.

53. Martínez-Lope, M. J.; Alonso, J. A.; Retuerto, M.; Fernández-Díaz, M. T. *Inorg. Chem.* **2008**, *47*, 2634.

54. Alonso, J. A.; Martínez-Lope, M. J.; Casais, M. T.; Fernández-Díaz, M. T. *Inorg. Chem.* **2000**, *39*, 917.

55. Jager, C.; Kunath, G.; Losso, P.; Scheler, G. *Solid State Nucl. Magn. Reson.* **1993**, *2*, 73.

56. Buannic, L.; Blanc, F.; Middlemiss, D.; Grey, C. P. *J. Am. Chem. Soc.* **2012**, *134*, 14483.

1
2
3
4
5
6
7
8
9
10
11
12
13
14
15
16
17
18
19
20
21
22
23
24
25
26
27
28
29
30
31
32
33
34
35
36
37
38
39
40
41
42
43
44
45
46
47
48
49
50
51
52
53
54
55
56
57
58
59
60

Figure 1 The crystal structure of $LaScO_3$ viewed (a) along the c axis and (b) across the ab plane. Green spheres represent the lanthanum atoms, and the ScO_6 octahedra are shown as polyhedra. Crystallographic data is taken from the literature.[10]

Figure 2 Conventional [45]Sc MAS NMR spectra for $LaScO_3$ at (a) 9.4 T and (b) 14.1 T. Also shown as inserts are expansions of the centreband in each spectrum. Shown in (c) and (d) are expansions of the satellite transition spinning sidebands, marked with *. Spectra are the result of averaging 96 and 32 transients, with a recycle interval of 5 s, for spectra acquired at 9.4 T and 14.1 T, respectively. Conventional [45]Sc MAS NMR spectra of $LaScO_3$ with a wide spectral width at (e) 9.4 T and (f) 14.1 T. Spectra are the result of averaging 192 transients with a recycle interval of 5 s. The MAS rate was 14 kHz and 10 kHz at 9.4 T and 14.1 T, respectively.
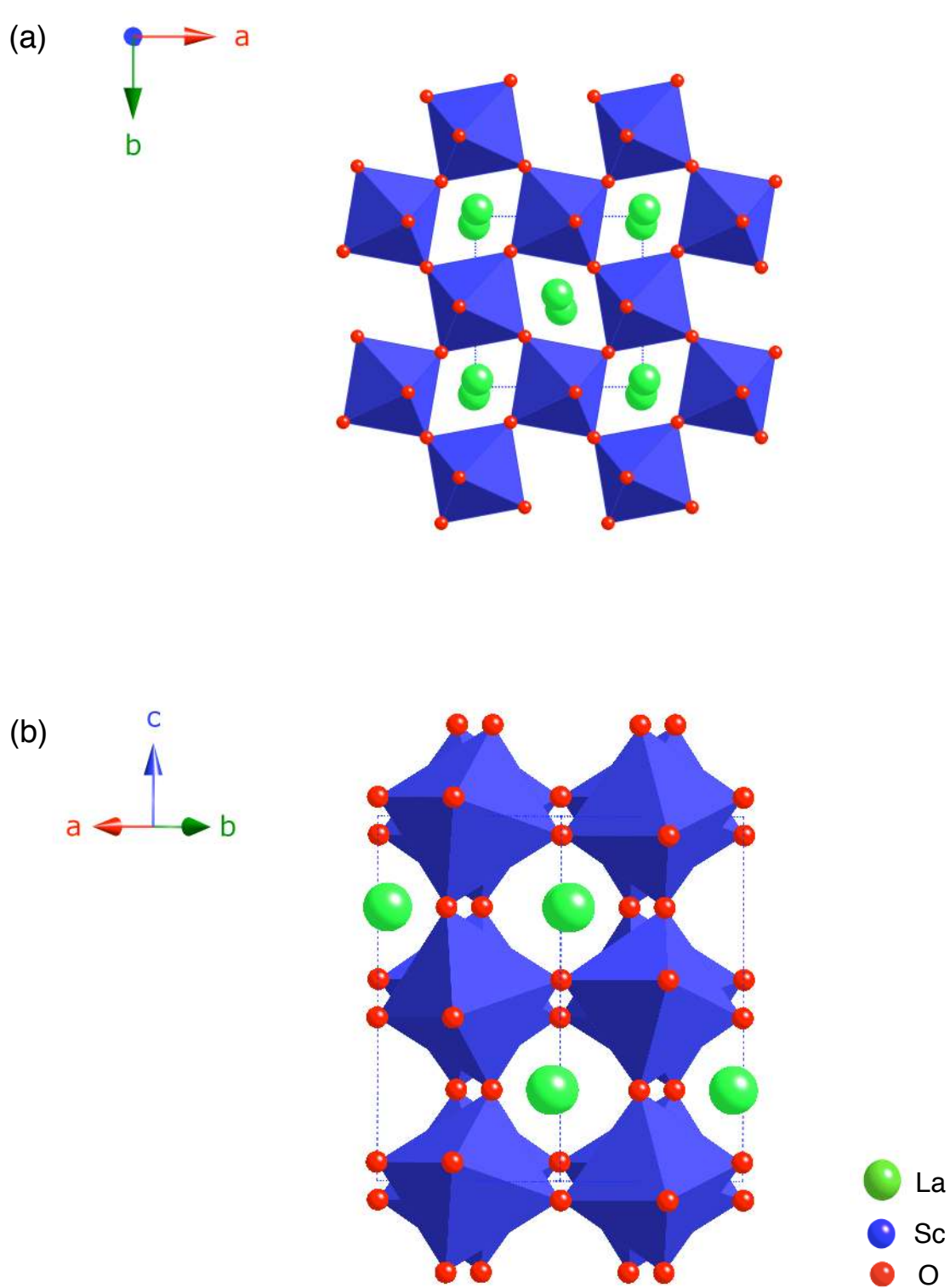
Figure 3 Conventional [45]Sc (14.1 T) MAS NMR spectra, triple-quantum MAS NMR spectra and corresponding projections for (a) $LaScO_3$ and (b) $YScO_3$. Spectra are the result of averaging 96 transients with a recycle interval of 3 s for each of the 256 increments of 20 µs. The MAS rate was 10 kHz.

Figure 4 Conventional [17]O (14.1 T) MAS NMR spectra of (a) $LaScO_3$ and (b) $YScO_3$. Also shown as inserts are expansions of the centreband in each spectrum. Spinning sidebands are marked with *. Spectra are the result of averaging (a) 576 and (b) 80 transients with a 20 s recycle interval. The MAS rate was 30 kHz.

Figure 5 (a) Static [89]Y (14.1 T) NMR spectrum of $YScO_3$ and conventional [89]Y (14.1 T) MAS NMR spectra of $YScO_3$ acquired at MAS rates of (b) 1.2 kHz and (c) 10 kHz. Spectra are the result of averaging (a) 1408 and (b,c) 720 transients with a recycle interval of 20 s.

Figure 6 Isolated ScO_6 octahedra for (a) $LaScO_3$ and (b) $YScO_3$ obtained from Rietveld refinement of NPD data, showing the Sc – O bond distances.

Figure 7 (a) Variation observed in the unit cell parameters a (diamonds), b (squares), c (circles) and the unit cell volume (triangles) with increasing x for $La_{1-x}Y_xScO_3$. Note that for

ease of comparison the c parameter has been divided by √2. The estimated error bars are smaller than the symbols used and are therefore not shown. (b) The variation observed in the tilt angle, ϕ, (circles) and orthorhombic strain, s, (squares) with increasing x in $La_{1-x}Y_xScO_3$. (c) The variation observed in the bond deviation, Δ_d, with increasing x for $La_{1-x}Y_xScO_3$.

Figure 8 Comparison of ^{45}Sc (a) 9.4 T and (b) 14.1 T MAS NMR spectra obtained for samples in the solid-solution $La_{1-x}Y_xScO_3$. Spectra are the result of averaging (a) 96 and (b) 24 transients with a recycle interval of (a) 5 s and (b) 3 s. The MAS rate was (a) 14 kHz and (b) 10 kHz.

Figure 9 Conventional ^{45}Sc (14.1 T) MAS NMR spectra, triple-quantum MAS NMR spectra and corresponding projections for (a) $La_{0.8}Y_{0.2}ScO_3$, (b) $La_{0.6}Y_{0.4}ScO_3$, (c) $La_{0.4}Y_{0.6}ScO_3$ and (d) $La_{0.2}Y_{0.8}ScO_3$. Spectra were recorded using a z-filtered pulse sequence. Also shown in (a) are axes highlighting the respective gradients along which samples exhibiting a distribution of chemical shift or quadrupolar interactions will lie. The MAS rate was 10 kHz. Spinning sidebands are denoted by *.

Figure 10 Conventional ^{89}Y (14.1 T) MAS NMR spectra recorded for compositions x = 0.2, 0.4, 0.6, 0.8 and 1 in the series $La_{1-x}Y_xScO_3$. Spectra are the result of averaging (a) 4096, (b) 3072, (c) 1080 and (d, e) 720 transients with a recycle intervals of 20 s. The MAS rate was 10 kHz.

Figure 11 (a) Simulated ^{45}Sc MAS NMR spectra obtained by 'summing' the NMR parameters from the ^{45}Sc DFT calculations completed for a single unit cell (1 × 1 × 1), shown in blue, and a 2 × 1 × 1 supercell, shown in purple. Also shown in green is the summation of the two simulated patterns. (b) The ^{89}Y (14.1 T) MAS NMR spectrum of $La_{0.6}Y_{0.4}ScO_3$ (Figure 10) with tick marks corresponding to the calculated chemical shifts of Y sites in a 1 × 1 × 1 single cell (shown in blue) and 2 × 1 × 1 supercell (shown in red) calculations.

TOC Graphic

1
2
3
4
5
6
7
8
9
10
11
12
13
14
15
16
17
18
19
20
21
22
23
24
25
26
27
28
29
30
31
32
33
34
35
36
37
38
39
40
41
42
43
44
45
46
47
48
49
50
51
52
53
54
55
56
57
58
59
60

(a)

(b)

La
Sc
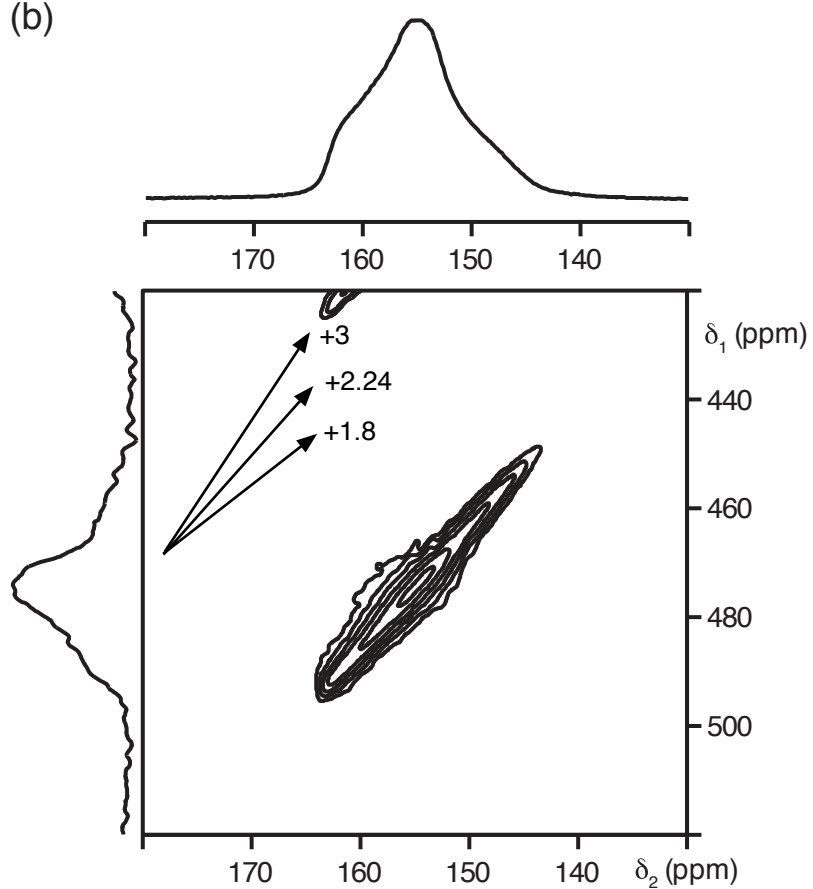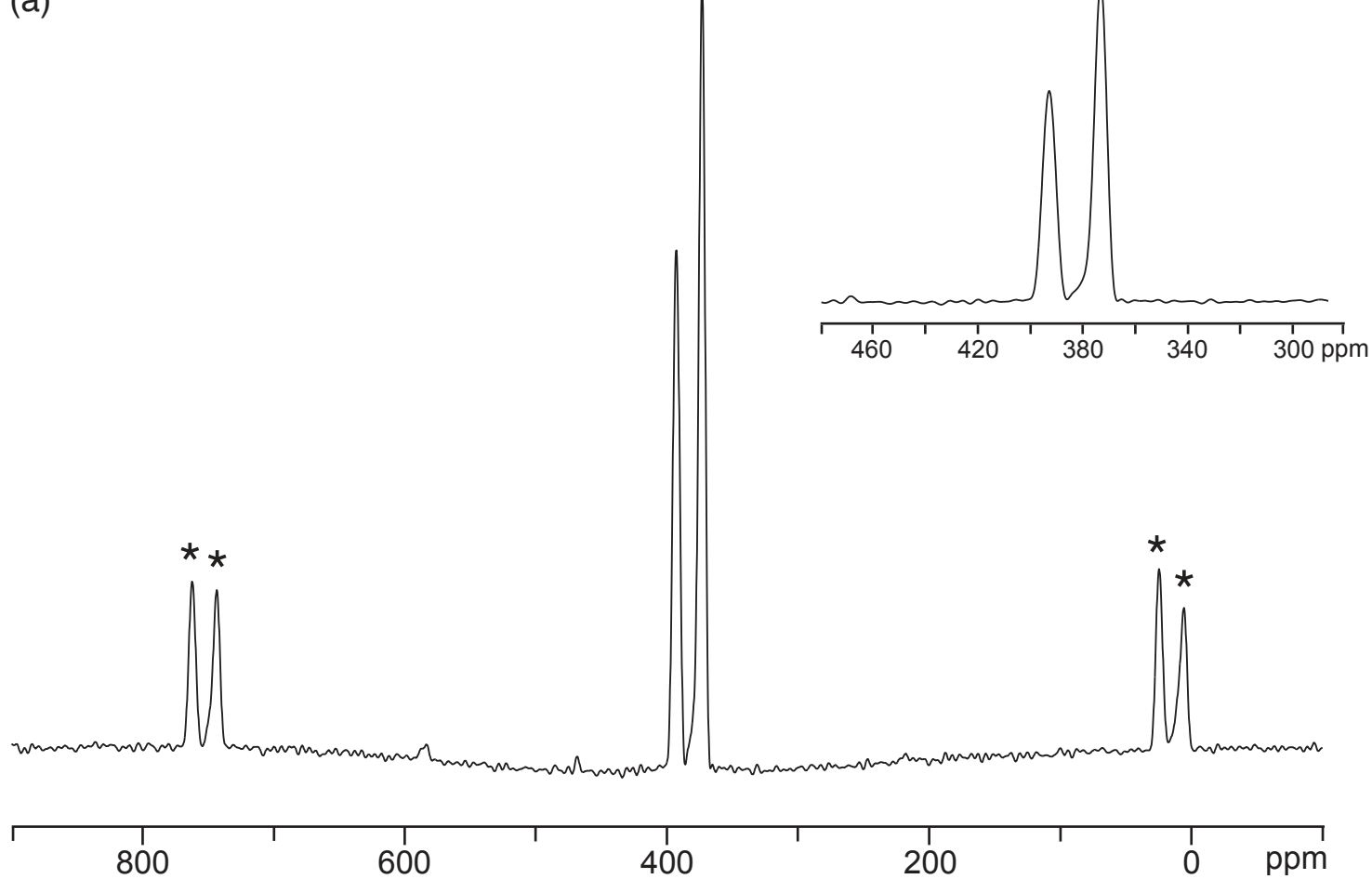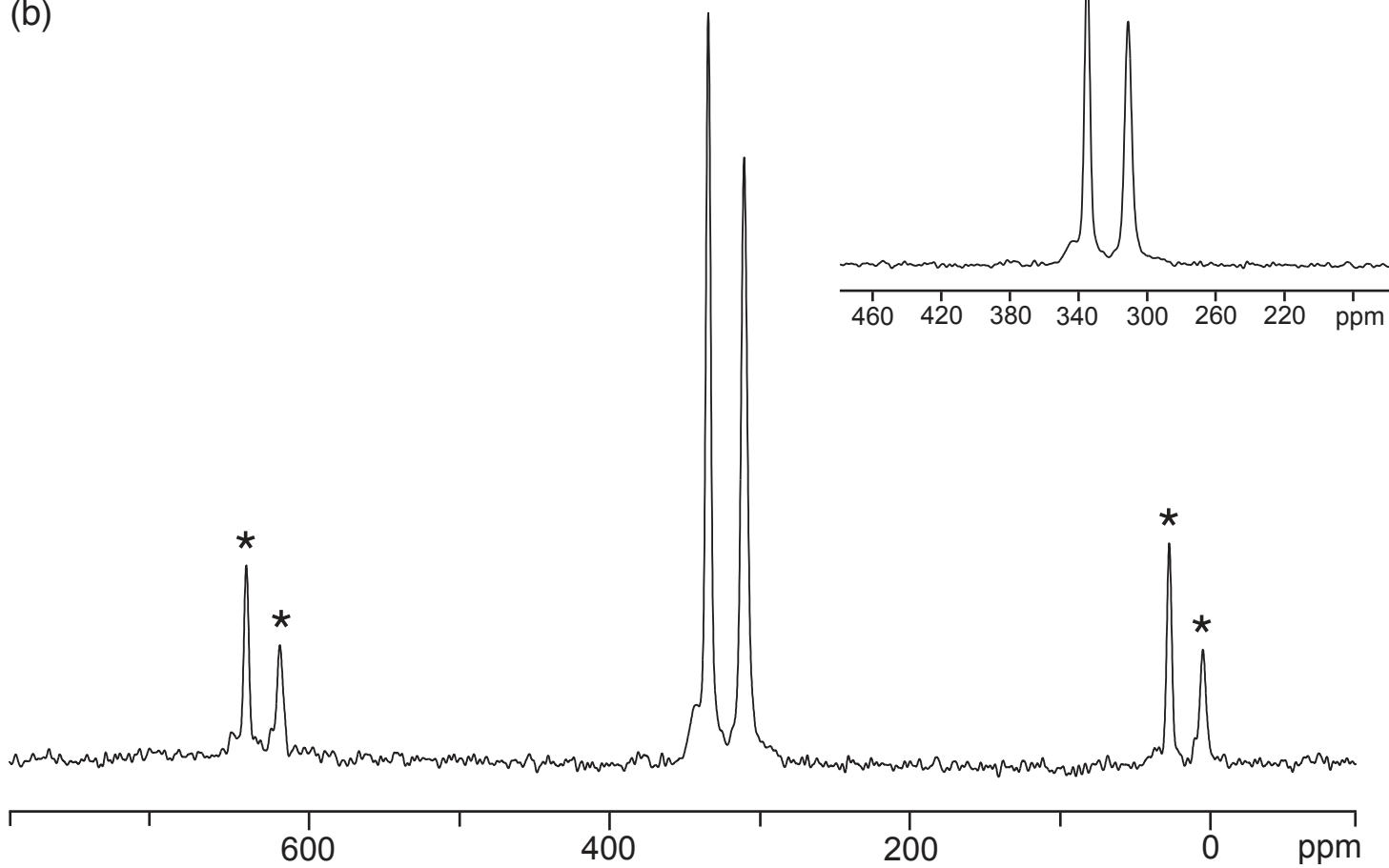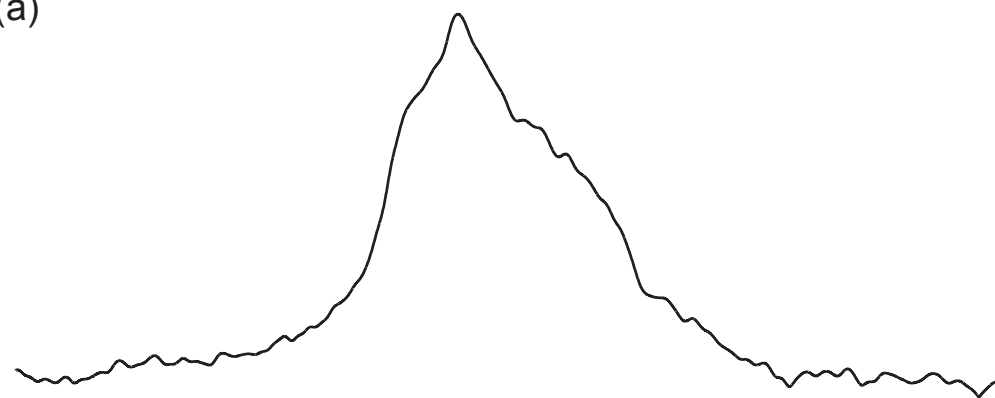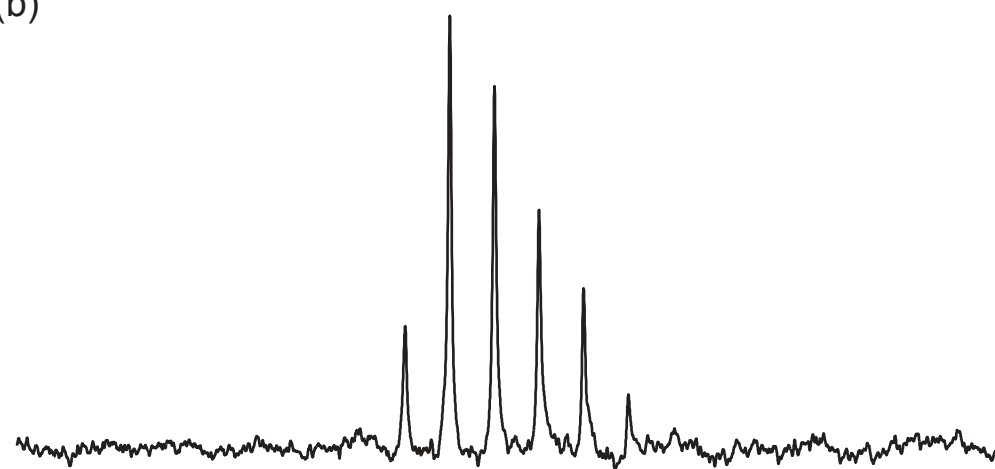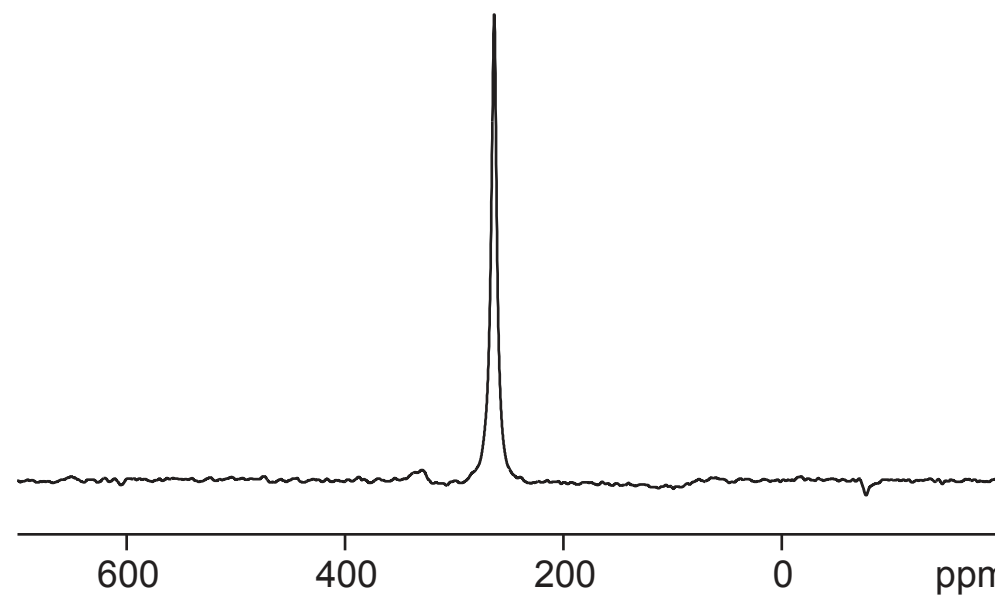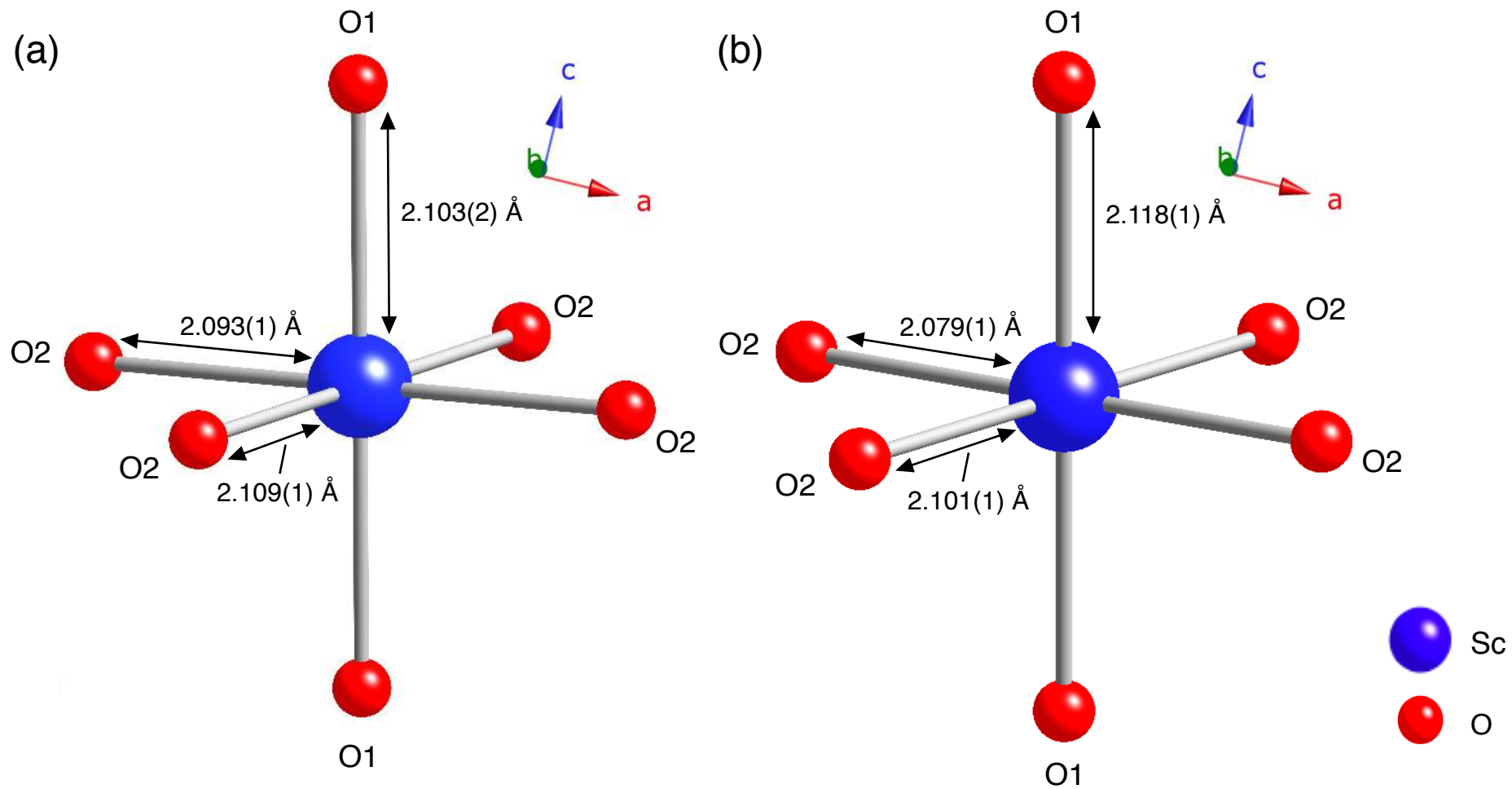O

9.4 T

14.1 T

(a)

190 180 170 160 150 140 ppm

* *

350   250   150   50   −50 ppm

(b)

190 180 170 160 150 140 ppm

* *

240   200   160   120   80 ppm

(c)

ST₁

ST₂

ST₃

60   40   20   0   −20 ppm

(d)

ST₁

ST₂

ST₃

115   105   95   85   75 ppm

(e)

4000   2000   0   −2000   −4000 ppm

(f)

3000   2000   1000   0   −1000 −2000 ppm

(a)

170   165   160   155

δ_1 (ppm)

+3

+2.24   460

+1.8   470

480

490

500

510

170   165   160   155 δ_2 (ppm)   520

(b)

170   160   150   140

δ_1 (ppm)

+3

+2.24   440
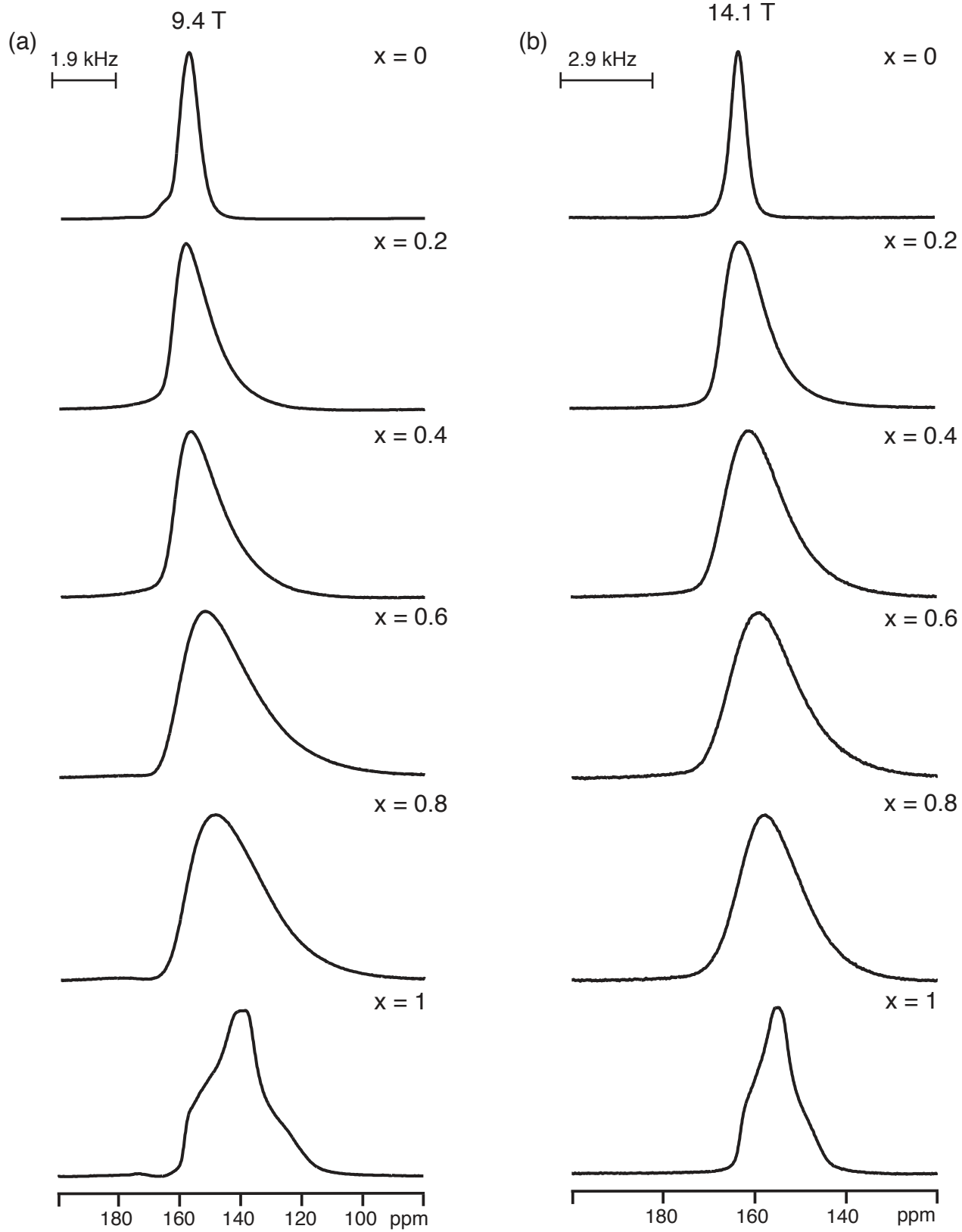
+1.8

460

480

500

170   160   150   140 δ_2 (ppm)

(a)

(b)

(c)

600   400   200   0   ppm

(a)

(b)

(c)

(a) x = 0.2

(b) x = 0.4

(c) x = 0.6

(d) x = 0.8

(e) x = 1

300   250   200   ppm

(a)

(b)